Brazilian Journal of Physics (2023) 53:135
https://doi.org/10.1007/s13538-023-01328-3

GENERAL AND APPLIED PHYSICS

Capillary Phenomena in Tubes Under Microgravity

Shangtong Chen[1] · **Di Wu**[2,3] · **Wen Li**[1] · **Fenglin Ding**[1] · **Qi Kang**[2,3] · **Yong Li**[1]

Received: 24 January 2023 / Accepted: 6 June 2023 / Published online: 3 August 2023

Abstract

Propellant tanks and propulsion systems are essential for space missions. Studying capillary phenomena of the liquid in tubes with varying cross-section under microgravity can provide the theoretical foundation for separating gas from liquid, saving propellant, and so on. In this study, a mathematical model for profiles of the liquid in tubes with varying cross-section under microgravity is obtained. With the given liquid contact angle and geometry of the tube, a model based on the shooting method is developed to predict profiles of the liquid. The length, interface area, and volume of the liquid ring can all be obtained according to the mathematical model. The theory is verified by numerical simulation in which, different geometries of the tube and different volumes and contact angles of the liquid are taken into account.

Keywords Capillary phenomena · Microgravity · Tubes · Shooting method

1 Introduction

In the microgravity environment, surface tension plays a major role, and the liquid can be spread on the tube's wall no matter how much its diameter is. Propellant tanks and propellant systems consist of plenty of tube structures. Studying behaviors of the liquid in tubes can provide the theoretical basis for separating gas from liquid, saving propellant, and so on.

Capillary phenomena from the static to the dynamic point of view have been widely studied. The famous Lucus-Washburn equation was obtained by adopting a balance between the capillary-driven force, the friction force and the gravity forces [1, 2]. Since then, capillary-driven flows in cylindrical tubes with uniform or nonuniform cross-section [3–7], oval tubes [8], noncircular tubes [9], complex containers [10], axisymmetric geometries [11], and concentric annuli [12] have been deeply analyzed, and the dynamic equations of flows in these containers have been proposed. Capillary-driven flows in corners were also comprehensively studied, including flows in the sharp inner corner [13–15], the corner formed by plates with varying wettability [16], the rounded interior corner [17], the corner formed by a plate and a rounded wall [18], and the curved interior corner [19]. Capillary rise of liquid between parallel plates was analyzed by Dreyer et al. [20] and was extended to the problems of liquid penetration in metal wire mesh between parallel plates [21] and the flow between plates with varying cross-section [22]. Theoretical analysis, drop tower experiments and numerical simulation of capillary driven flows have been used to optimize the propellant management device (PMD) and analyze liquid behaviors in tanks [23–26].

Static capillary surfaces in containers and corners were studied and the well-known Concus-Finn condition was proposed [27]. Carroll [28] derived theoretical expressions of profiles of liquid drops on cylindrical fibers. And it was extended to liquid drops on fibers with varying cross-sections by Chen et al. [29]. Michielsen et al. [30] explored liquid drops on conical fibers and proposed a method based on minimizing the Gibbs free energy to predict profiles of liquid drops. Profiles of liquid drops at the bottom of cylindrical fibers standing on flat substrates [31] and at the tips of cylindrical fibers [32] were obtained by Du et al. Liquid bridges were widely studied, such as liquid bridges between parallel plates, between two spheres, or between a plane and a cylindrical wall [33–39]. Capillary surfaces in cubes [40], polyhedral containers [41] and truncated-cone-shaped

---

✉ Yong Li
li-y95@tsinghua.org.cn

[1] Beijing Institute of Control Engineering, China Academy of Space Technology, Beijing 100094, China

[2] Institute of Mechanics, Chinese Academy of Sciences, Beijing 100190, China

[3] College of Engineering and Science, University of Chinese Academy of Sciences, Beijing 100049, China

containers [42] were analyzed too. The hydrodynamic stability of constrained capillary surfaces was comprehensively analyzed by Bostwick and Steen [43].

However, profiles of liquid drops in tubes with varying cross-section under microgravity have not been obtained yet. In this study, through theoretical derivation, the mathematical model for the profiles of liquid drops is obtained. With the given liquid contact angle and geometry of the tube, profiles of liquid drops can be predicted with the shooting method. Numerical simulations are performed with the volume of fluid (VOF) method in Fluent by considering different diameters of the tube and different volumes and contact angles of the liquid. Comparisons of r_2 and V_l between theoretical and numerical results are presented and they are quite consistent with each other. Moreover, influences of the contact angle and the volume of liquid on the profiles are discussed in detail.

2 Derivation of the Theoretical Model

Figure 1 shows the vertical cross-sectional view of the model. The blue region represents the liquid and the black curves represent the tube's wall. The liquid is spread around the tube's wall. The cylindrical coordinate is used for analysis in this study. The z axis is the axis of symmetry of the tube and the r axis is perpendicular to the z-axis. The liquid profile is symmetric with respect to both of the z and r axes, so the analysis is conducted in the first quadrant of the model. The two end points of the profile curve in the first quadrant are Point $A(r_1, z_1)$ and Point $B(r_2, 0)$. Point A locates on the tube's wall and Point B locates on the r axis.

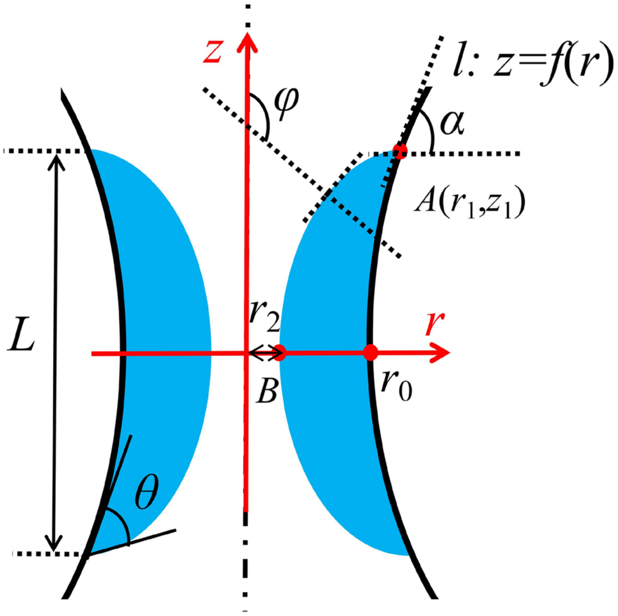

Fig. 1 Vertical cross-sectional view of the model

φ is the angle between the positive direction of the z axis and the normal to the profile curve of the liquid. L is the length of the liquid drop. The liquid contact angle on the wall of the tube is θ. The profile of the tube's wall can be expressed as a function of r, $f(r)$. When $z=0$, the radius of the tube is r_0.

A continuous, differentiable curve at any reference point can be described by its local tangent and its curvature $K=1/R$. A smooth surface can be described at any reference point by its tangential plane and the two principal curvatures $K_1=1/R_1$ and $K_2=1/R_2$, written as

$$K_1 = -\frac{d}{dr}\frac{dz/dr}{\sqrt{1+(dz/dr)^2}} \tag{1}$$

$$K_2 = -\frac{1}{r}\frac{dz/dr}{\sqrt{1+(dz/dr)^2}} \tag{2}$$

According to the Young–Laplace equation $K_1+K_2=Constant$. The expression of the profile curve of the liquid can be obtained by adding up the two main curvatures, which leads to

$$\frac{1}{r}\frac{d}{dr}\frac{rdz/dr}{\sqrt{1+(dz/dr)^2}} = C_1 \tag{3}$$

where C_1 is a constant. The radial component of the normal to the surface equals the sine of the angle φ. Multiplying Eq. (3) by r, the first integral of Eq. (3) can be obtained as below

$$\frac{rdz/dr}{\sqrt{1+(dz/dr)^2}} = r\sin\phi = \frac{C_1}{2}r^2 + C_2 \tag{4}$$

where C_2 is also a constant. The boundary conditions are

$$\begin{gathered} r = r_1, \cdots \varphi = \pi + \theta - a, a = \arctan \dot{f}_{r=r_1} \\ r = r_1, \cdots \varphi = \pi/2 \end{gathered} \tag{5}$$

where $\dot{f}$ means df/dr. By combining Eqs. (4) and (5), we can determine C_1 and C_2 as follows:

$$C_1 = -\frac{2\left[r_1\sin(\theta-\alpha)+r_2\right]}{r_1^2-r_2^2} \tag{6}$$

$$C_2 = \frac{r_1^2r_2 + r_1r_2^2\sin(\theta-\alpha)}{r_1^2-r_2^2} \tag{7}$$

For the gradient of the profile curve of the liquid, dz/dr, there exists a relationship as below

$$-\frac{dz}{dr} = \tan\phi = \frac{\sin\phi}{-\left(1-\sin^2\phi\right)^{0.5}} \tag{8}$$

The denominator on the right hand side of Eq. (8) is negative because φ is greater than π/2. We combine Eqs. (4)–(8) to obtain the expression of the gradient of the profile curve, which is a function of r, and after simplification, we have the expression as below

$$\frac{dz}{dr} = -\frac{r^2\left[r_1 \sin(\theta-\alpha)+r_2\right]+r_1r_2\left[r_1+r_2\sin(\theta-\alpha)\right]}{\left\{r^2\left[r_1\sin(\theta-\alpha)+r_2\right]^2\left(r_2^2-r^2\right)-r_1^2\left[r_1+r_2\sin(\theta-\alpha)\right]^2\left(r_2^2-r^2\right)\right\}^{0.5}} \tag{9}$$

Writing

$$\mathrm{a} = -\frac{r_1+r_2\sin(\theta-\alpha)}{r_1\sin(\theta-\alpha)+r_2} \tag{10}$$

Equation (7) can be transformed into the form

$$\frac{dz}{dr} = -\frac{r^2+ar_1r_2}{\left[\left(r_2^2-r^2\right)\left(r^2-a^2r_1^2\right)\right]^{0.5}} \tag{11}$$

If r_1 and r_2 are both known, Eqs. (9) and (11) can be solved numerically with the ode45 method or the Runge–Kutta method and the expression of the profile can be obtained.

The length L of the liquid ring and the volume of liquid V_l are the major concerned parameters. They can both be obtained according to the theoretical solutions proposed above. When the coordinate values of Point A are obtained, L will be determined. The volume of liquid is expressed as

$$V_1 = V_t - V_g \tag{12}$$

where V_l is the volume of liquid, V_t is the volume of the tube with a height of L, V_g is the volume of gas, whose expressions are written as follows:

$$V_t = 2\pi\int_0^{z_1} r^2 dz \tag{13}$$

$$V_g = 2\pi\int_0^{z_1} r^2 dz = -2\pi\int_{r_2}^{r_1} r^2\frac{r^2+ar_1r_2}{\left[\left(r_2^2-r^2\right)\left(r^2-a^2r_1^2\right)\right]^{0.5}}dr \tag{14}$$

3 Numerical Simulation

Numerical simulation is performed in Fluent with the VOF method. Tubes with different sizes and a kind of silicone oil named by its kinematic viscositiy (2 cSt) are used to establish the model in our study. The properties of 2 cSt are shown in Table 1. Figure 2 shows a mesh model of the tube with varying cross-section. Grid independence verification has been carried out and the appropriate number of grids is chosen. Boundary layers are established near the tube's wall and the expansion ratio between two adjacent layers is 1.2.

Table 1 Liquid properties (25 ℃)

Liquid	μ (kg/(m*s))	ρ (kg/m^3)	σ (N/m)	ν (10^{-6} m^2/s)
2 cSt	0.001746	873	0.0183	2

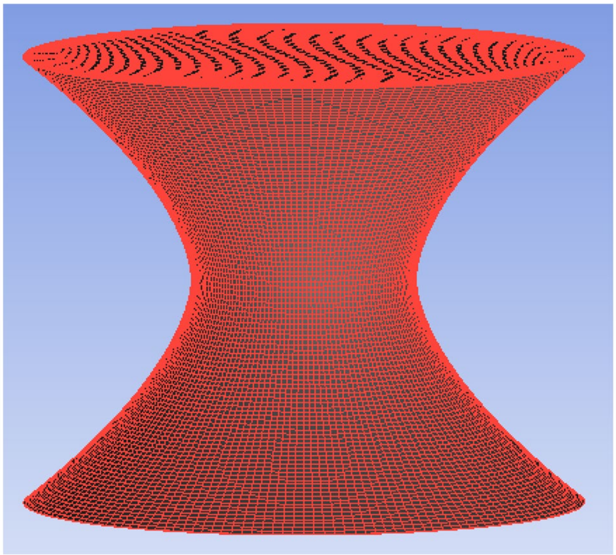

Fig. 2 3D Mesh model of a tube with varying cross-section

Numerical settings are shown in Table 2. As the *Re* number during the re-orientation process of liquid is much smaller than 2000, laminar flow is assumed. The time-step size is 0.0005 s and the simulation result is saved automatically every 1500 steps. The calculation time is long enough to make sure that the liquid in the tube has reached the equilibrium state. The calculation process is very stable because the *Courant* number is much smaller than 1.

At initial time, the liquid forms a liquid column in the tube, as shown in Fig. 3, in which the red region represents the liquid. If the volume of liquid is within a certain range,

Table 2 Numerical settings

Equations	Settings
Pressure–velocity coupling equation	SIMPLEC
Spatial discretization of the pressure equation	Body force weighted
Spatial discretization of the volume fraction equation	Geo-reconstruct
Spatial discretization of the momentum equation	Second-order upwind scheme
Spatial discretization of the gradient equation	Least square cell

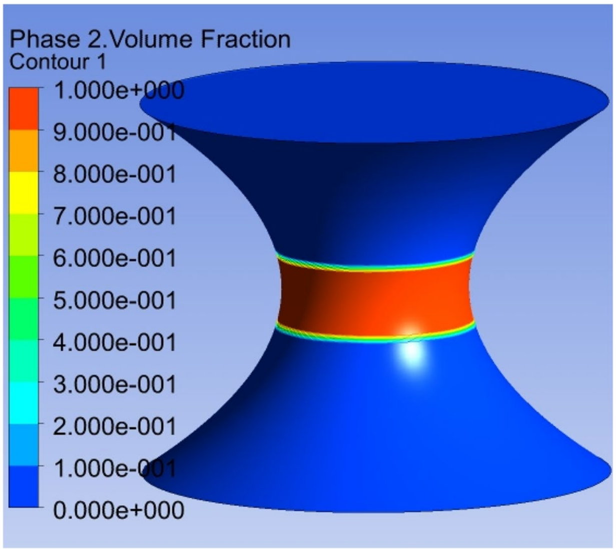

Fig. 3 Initial liquid distribution

the liquid will form a section of liquid ring and spread around the tube's wall at equilibrium, as shown in Fig. 4a, b, in which the yellow surface stands for the liquid–gas interface at equilibrium. In this case, the liquid–gas interface is similar to that of the liquid bridge. If the volume of liquid is too big, the liquid will appear as a liquid column and form a liquid seal at equilibrium. In this case, the liquid–gas interface is part of a sphere. If the volume of liquid is not big enough, the liquid will form one or some liquid drops and attach to the tube's wall at equilibrium. Unfortunately, the critical volumes of liquid between these three liquid phases are not found in this paper. The other kinds of liquid–gas interfaces except the liquid-ring interface are not discussed further in this paper.

4 Results and Analysis

The geometry of the tube, the volume of liquid and the liquid contact angle are given at first in the simulation. We measure the coordinate values of points A and B from the numerical results and compare them with the theoretical predictions. We measure two sets of data of points on the profile curves on two orthogonal cross-sections that pass the axis of the tube respectively at a moment when the liquid is at equilibrium, and take the average values of these two sets of data as the final results. Theoretical predictions are obtained by using the shooting method combined with Eqs. (11)–(14). When V_l is known, r_1 is firstly estimated to be in a given range and r_2 is assumed an estimated value. We calculate the volume of liquid based on r_1 and r_2 iteratively according to Eqs. (11)–(14) until the difference between the calculated volume and the given value of V_l is less than $1\mathrm{e}^{-5}$. During this process, r_1 is guaranteed to locate on the tube's wall. When r_2 is known, it is substituted into the mathematical model at first. Then r_1 is adjusted within a given range until it locates on the tube's wall. After r_1 is determined through the shooting method, theoretical predictions of the profile and the volume of liquid are obtained.

Numerical and theoretical results are shown in Table 3. The ratios of theoretical results to numerical results of V_1 and r_2 are also presented in Table 3. The values of ratios are mostly between 95 and 105%. To give a more intuitive observation, these ratios are plotted in Fig. 5.

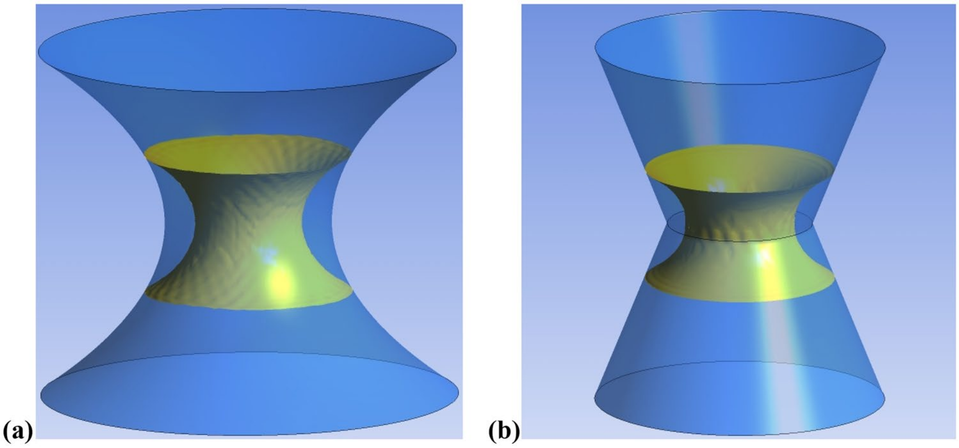

Fig. 4 Liquid–gas interfaces at equilibrium. **a** $\theta=30°$, $f=80/60^{0.5}*(r\text{-}40)^{0.5}$ mm. **b** $\theta=40°$, $f=2.5(r\text{-}40)$ mm

Table 3 Model parameters, numerical results and theoretical predictions based on the shooting method

	Parameters				Numerical results			Theoretical predictions for given V_l				Theoretical predictions for given r_2			
No	r_0 [mm]	Expressions of tube wall's profile [mm]	θ [°]	V_l [mm^3]	r_l [mm]	z_l [mm]	r_2 [mm]	r_l [mm]	z_l [mm]	r_2 [mm]	Ratios of theoretical to numerical results of r_2 [%]	r_l [mm]	z_l [mm]	V_l [mm^3]	Ratios of theoretical to numerical results of V_l [%]
#1	20	$r=20$	30	22,619	20	21.37	11.86	/	21.50	12.25	103.3	/	22.00	24,015	106.2
#2	20	$r=20$	40	22,619	20	18.72	10.56	/	18.56	10.85	102.7	/	18.81	23,420	103.5
#3	20	$r=20$	50	20,106	20	15.61	10.66	/	15.55	10.42	97.75	/	15.36	19,539	97.18
#4	40	$r=40$	30	201,060	40	44.91	21.60	/	44.76	23.02	106.6	/	46.07	218,420	108.6
#5	40	$r=40$	50	150,800	40	31.13	22.05	/	30.26	21.84	99.05	/	30.07	148,740	98.63
#6	40	$r=40$	70	100,530	40	19.85	23.50	/	19.95	23.02	97.96	/	19.57	96,712	96.20
#7	60	$r=60$	40	452,390	60	48.20	39.19	/	48.89	38.28	97.68	/	49.03	459,510	101.6
#8	60	$r=60$	50	452,390	60	42.78	35.37	/	43.08	35.12	99.29	/	42.81	446,610	98.72
#9	60	$r=60$	60	339,290	60	34.83	37.30	/	33.51	37.10	99.46	/	33.30	335,290	98.82
#10	80	$r=80$	30	1,407,400	80	85.50	50.15	/	84.99	49.72	99.14	/	84.38	1,383,800	98.32
#11	80	$r=80$	40	1,206,400	80	69.43	47.86	/	68.74	48.44	101.2	/	69.47	1,236,100	102.5
#12	80	$r=80$	70	804,250	80	38.73	47.07	/	39.88	46.04	97.81	/	39.06	770,390	95.79
#13	20	$z=4(r\text{-}20)$	30	25,260	25.50	22.05	14.14	25.39	21.60	13.91	98.37	25.31	21.23	24,196	95.79
#14	20	$z=4(r\text{-}20)$	45	19,177	23.79	15.20	13.29	23.78	15.11	13.02	97.97	23.70	14.78	18,206	94.94
#15	40	$z=2.5(r\text{-}40)$	40	174,547	53.30	33.30	28.05	53.12	32.80	28.11	100.2	53.14	32.86	175,531	100.6
#16	40	$z=2.5(r\text{-}40)$	35	174,547	54.43	36.11	30.04	54.37	35.93	29.89	99.50	54.27	35.69	171,498	98.25
#17	20	$z=8{*}5^{0.5}(r\text{-}20)^{0.5}$	30	20,241	21.74	20.20	13.01	21.21	19.67	12.70	97.62	21.16	19.24	19,153	94.62
#18	20	$z=8{*}5^{0.5}(r\text{-}20)^{0.5}$	40	17,683	21.30	16.87	12.63	20.81	16.13	12.32	97.55	20.78	15.75	16,727	94.59
#19	40	$z=5{*}10^{0.5}(r\text{-}40)^{0.5}$	20	174,224	49.33	44.10	25.87	47.89	44.41	26.44	102.2	48.10	45.01	182,306	104.6
#20	40	$z=5{*}10^{0.5}(r\text{-}40)^{0.5}$	40	174,224	45.26	32.07	21.47	44.31	32.84	21.04	98.00	44.25	32.59	170,139	97.66
#21	40	$z=80/60^{0.5}(r\text{-}40)^{0.5}$	20	156,182	53.42	37.81	26.60	53.51	36.96	27.28	102.3	53.94	38.56	165,726	106.1
#22	40	$z=80/60^{0.5}(r\text{-}40)^{0.5}$	30	156,182	49.97	32.42	24.80	49.88	32.46	24.97	99.68	49.66	32.10	153,852	98.51
#23	40	$z=80/60^{0.5}(r\text{-}40)^{0.5}$	40	134,182	47.15	27.30	24.43	46.73	26.79	24.12	97.73	46.62	26.58	130,925	97.57
#24	40	$z=80/60^{0.5}(r\text{-}40)^{0.5}$	50	123,379	45.03	22.76	24.16	44.94	22.96	22.98	94.10	44.64	22.26	112,685	91.33
#25	60	$z=120/90^{0.6}(r\text{-}60)^{0.6}$	20	478,665	85.37	54.96	46.41	86.33	57.40	46.25	99.66	86.14	57.15	471,841	98.57
#26	60	$z=120/90^{0.6}(r\text{-}60)^{0.6}$	30	478,665	78.60	46.21	42.65	78.91	47.07	41.60	97.54	78.98	47.16	462,253	96.57
#27	60	$z=120/90^{0.6}(r\text{-}60)^{0.6}$	40	426,929	73.51	38.74	40.09	73.60	38.62	39.25	101.3	73.77	38.91	436,499	102.2

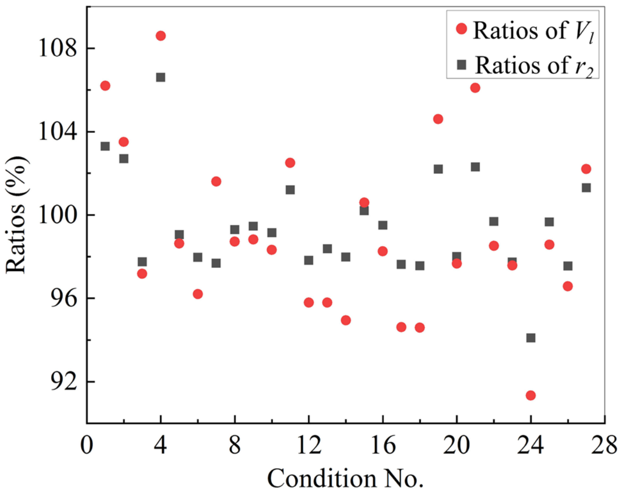

Fig. 5 Ratios of theoretical predictions to numerical results

The abscissa represents the number of conditions and the ordinate represents the ratio values. The black squares stand for the ratio values calculated for r_2 and the red dots represent the ratio values calculated for V_l. It can be seen that the most of the ratios are around 100%, which indicates that numerical results are in good agreement with theoretical ones.

A tube with uniform cross-section is the most common condition. We take it as an example for further analysis. To compare profiles of the liquid obtained through numerical simulations and theoretical predictions more comprehensively and intuitively, we take the coordinate values of a series of points on the simulated liquid surface and plot them together with theoretical results in Fig. 6. The figure shows profiles of the liquid in the tube with $r_0 = 80$ mm. Condition numbers, #10, #11, #12, are labeled on the top-left corner of the figure, which are consistent with those in Table 3. The horizontal and vertical axes represent r and z respectively. The curves are theoretical profiles and the dots stand for numerical results. It shows that numerical results of the profiles are in good agreement with theoretical predictions.

For tubes with uniform cross-section, Eq. (11) can be transformed into

$$\frac{dz}{dr} = -\frac{r^2 + ar_1r_2}{\left[\left(r_2^2 - r^2\right)\left(r^2 - a^2r_1^2\right)\right]^{0.5}} \tag{15}$$

where $a = \left(r_1 - r_2\cos\theta\right)/\left(r_1\cos\theta - r_2\right)$.

For further analysis, Eq. (15) is recast in the dimensionless form

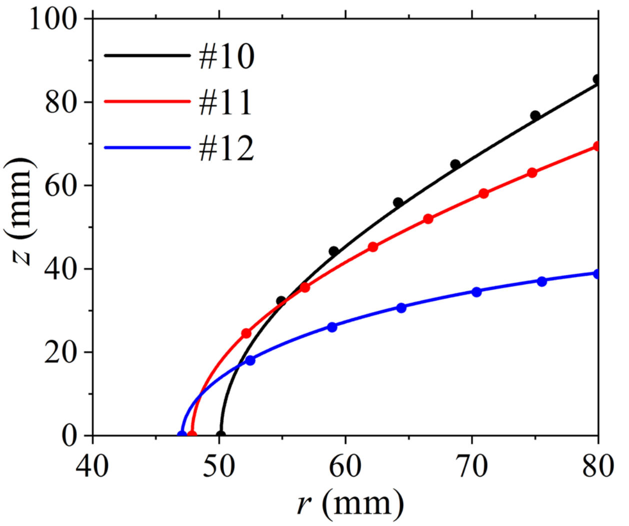

Fig. 6 Comparison between theoretical predictions and numerical results. The condition No. is #10, #11 and #12 in Table 3

$$\frac{d\bar{z}}{d\bar{r}} = -\frac{\bar{r}^2 + \bar{a}\bar{r}_2}{\left[\left(\bar{r}_2^2 - \bar{r}^2\right)\left(\bar{r}^2 - \bar{a}^2\right)\right]^{0.5}} \tag{16}$$

where $\bar{a} = \frac{1-\bar{r}_2\cos\theta}{\cos\theta-\bar{r}_2}$, $\bar{r}_2 = r_2/r_1$ and $\bar{z}_1 = z_1/r_1$.

The dimensionless volume of liquid is expressed as follows:

$$\bar{V}_l = \bar{V}_t - \bar{V}_g \tag{17}$$

$$\bar{V}_t = 2\pi\bar{z}_1 \tag{18}$$

$$\bar{V}_g = 2\pi\int_{\bar{r}_2}^{1}\bar{r}^2\frac{\bar{r}^2 + \bar{a}\bar{r}_2}{\left[\left(\bar{r}_2^2 - \bar{r}^2\right)\left(\bar{r}^2 - \bar{a}^2\right)\right]^{0.5}}d\bar{r} \tag{19}$$

When $\bar{r}_2$ is constant, the dimensionless length $\bar{L}$ and volume $\bar{V}_l$ vs the contact angle of the liquid are shown in Fig. 7a, b, respectively. The values of $\bar{r}_2$ are designed to be 0.5, 0.6, and 0.7. When r_2 is kept constant, both of the dimensionless length and volume of liquid decrease monotonically with the increasing contact angle of the liquid.

Profiles of the liquid under given values of $\bar{r}_2$ and $\bar{V}_l$ are shown in Fig. 8a, b, respectively. Curves with different colors stand for profiles of the liquid under different contact angles of the liquid. In Fig. 8a, $\bar{r}_2$ is 0.5 and, in Fig. 8b, $\bar{V}_l$ is 3. When $\bar{r}_2$ is kept constant, the smaller the contact angle, the higher position the profile curve will have, which

Fig. 7 **a** Dimensionless length $\overline{L}$ vs contact angle and **b** dimensionless volume $\overline{V}_l$ vs contact angle, with $\overline{r}_2$ constant.

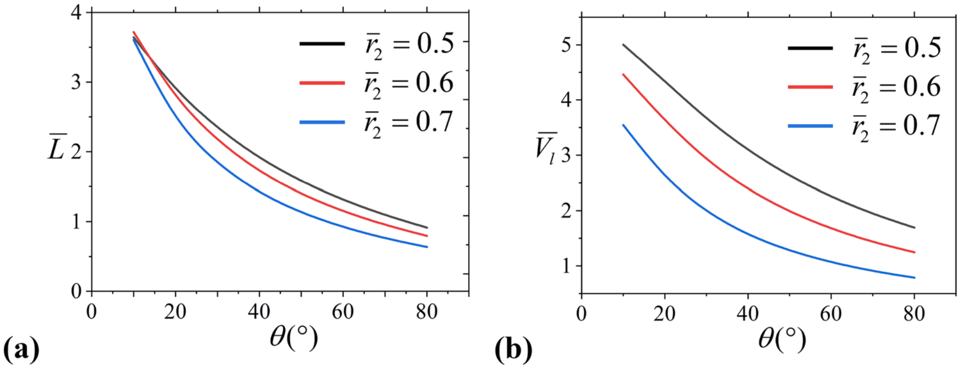

Fig. 8 Profiles of the liquid under different contact angles **a** $\overline{r}_2 = 0.5$ and **b** $\overline{V}_l = 3$

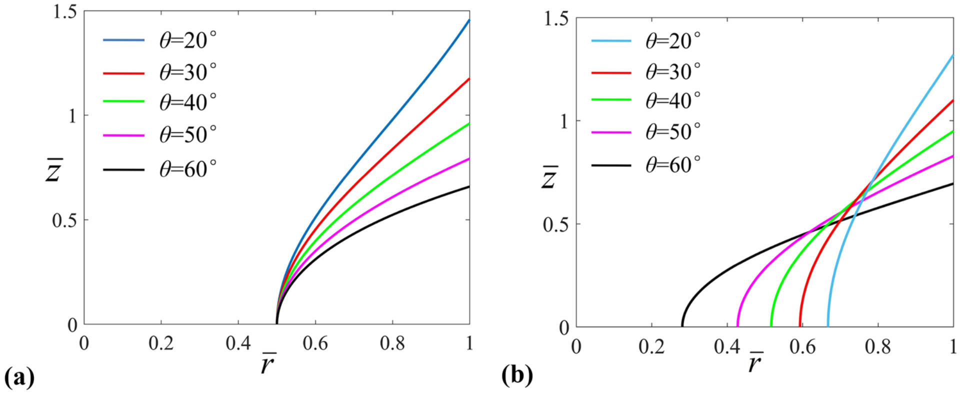

is consistent with Fig. 7a. When $\overline{V}_l$ is kept constant, $\overline{r}_2$ will decrease as the contact angle decreases. The profile curve will have higher position when the contact angle decreases.

5 Conclusions

Theoretical expressions of profiles of the liquid in a tube with varying cross-section under microgravity are obtained in this study. With the given liquid contact angle and geometry of the tube, profiles of the liquid can be predicted accurately with the model based on the Shooting method proposed in this study. Different geometries of the tube, different contact angles of liquid and different volumes of liquid are considered in the numerical simulation performed with the VOF method. And numerical results are in good agreement with theoretical predictions. Moreover, we take the coordinate values of a series of points on the profile curves from the simulated results and plot them together with profile curves predicted by the theoretical model in the figure, and we can see that they are in good agreement with each other. The dimensionless forms of profile and volume of the liquid are also presented in this study, and the tube with uniform cross-section is analyzed in detail as an example. When r_2 is kept constant, the length of the liquid ring L and the volume of liquid V_l keep increasing as the liquid contact angle decreases. When V_l is kept constant, L and r_2 keep increasing as the liquid contact angle decreases. The mathematical model and the method proposed in this study will be helpful for liquid management in space, which can provide the theoretical foundation for separating gas from liquid, saving propellant, and so on.

Funding This research was funded by the China Manned Space Engineering Program (Fluid Physics Experimental Rack and the Priority Research Program of Space Station), and the Natural Science Foundation Project (No. 12032020).

Data Availability The data presented in this study are available on request from the corresponding author.

Declarations

Ethics Approval Not applicable, no experiment has been conducted on human or animals.

Conflict of Interest The authors declare no competing interests.

References

1. R. Lucas, Rate of capillary ascension of liquids. Kolloid Z. **23**(7), 15–22 (1918)
2. E.W. Washburn, The dynamics of capillary flow. Phys. Rev. **17**, 273–283 (1921)
3. S. Levine, P. Reed, E.J. Watson, G. Neale, A theory of the rate of rise of a liquid in a capillary. Colloid and Interface Sci. **3**, 403–419 (1976)
4. M. Stange, M. Dreyer, H. Rath, Capillary driven flow in circular cylindrical tubes. Phys. Fluids **15**, 2587–2601 (2003)
5. J. Lei, Z. Xu, F. Xin, T. Lu, Dynamics of capillary flow in an undulated tube. Phys. Fluids **33**(5), 052109 (2021)
6. B. Figliuzzi, C.R. Buie, Rise in optimized capillary channels. J. Fluid Mech. **731**, 142–161 (2013)
7. J.C. Lei, H. Sun, S. Liu, S. Feng, T. Lu, Hypergravity effect on dynamic capillary flow in inclined conical tubes with undulated inner walls. Microgravity Sci. Technol. **34**, 71 (2022)
8. S. Chen, Z. Ye, L. Duan, Q. Kang, Capillary driven flow in oval tubes under microgravity. Phys. Fluids **33**, 032111 (2021)
9. R.M. Turian, F.D. Kessler, Capillary flow in a noncircular tube. AIChE J. **46**(4), 695–706 (2000)
10. A.B. Daniel, Y. Chen, B. Semerjian, N. Tavan, M.M. Weislogel, Compound capillary flows in complex containers: drop tower test results. Microgravity Sci. Technol. **22**, 475–485 (2010)
11. R. Chassagne, F. Dörflfler, M. Guyenot, J. Harting, Modeling of capillary-driven flows in axisymmetric geometries. Comput. Fluids **178**, 132–140 (2019)
12. S. Chen, Y. Chen, L. Duan, Q. Kang, Capillary rise of liquid in concentric annuli under microgravity. Microgravity Sci. Technol. **34**, 30 (2022)
13. M.M. Weislogel, S. Lichter, Capillary flow in an interior corner. J. Fluid Mech. **373**, 349–378 (1998)
14. Y. Tian, Y. Jiang, J.J. Zhou, M. Doi, Dynamics of Taylor rising. Langmuir **35**, 5183–5190 (2019)
15. M.M. Weislogel, J.T. McCraney, The symmetric draining of capillary liquids from containers with interior corners. J. Fluid Mech. **859**, 902–920 (2018)
16. M.M. Weislogel, C.L. Nardin, Capillary driven flow along interior corners formed by planar walls of varying wettability. Microgravity Sci. Technol. **17**(3), 45–55 (2005)
17. Y. Chen, M. Weislogel, C. Nardin, Capillary driven flows along rounded interior corners. J. Fluid Mech. **556**, 235–271 (2006)
18. Y.Q. Li, M.Z. Hu, L. Liu, Y. Su, L. Duan, Q. Kang, Study of capillary driven flow in an interior corner of rounded wall under microgravity. Microgravity Sci. Technol. **27**, 193–205 (2015)
19. Z.Y. Wu, Y. Y. Huang, X.Q. Chen, X. Zhang, Capillary driven flows along curved interior corners. I .J. Multiphase Flow. **109**, 14–25 (2018)
20. M. Dreyer, A. Delgado, H.J. Rath, Capillary rise of liquid between parallel plates under microgravity. J. Colloid Interface Sci. **163**, 158–168 (1994)
21. N. Weng, Q.G. Wang, J.D. Li, J. Lyu, H. Zhang, W. Yao, Liquid penetration in metal wire mesh between parallel plates under normal gravity and microgravity conditions. Appl. Therm. Eng. **167**, 114722 (2019)
22. S. Chen, L. Duan, Y. Li, F. Ding, J. Liu, W. Li, Capillary phenomena between plates from statics to dynamics under microgravity. Microgravity Sci. Technol. **34**, 70 (2022)
23. J. Li, H. Lin, K. Li, J. Zhao, W. Hu, Liquid sloshing in partially filled capsule storage tank undergoing gravity reduction to low/micro-gravity condition. Microgravity Sci. Technol. **32**, 587 (2020)
24. D. Zhang, L.Y. Meng, Numerical simulation analysis of liquid transportation in capsule-type vane tank under microgravity. Microgravity Sci. Technol. **32**, 817 (2020)
25. L. Wang, X. Zhang, Y. Yun, J. Liu, W. Li, B. Huang, Numerical simulation of the reorientation process under different conditions in a vane-type surface tension propellant tank. Microgravity Sci. Technol. **34**, 37 (2022)
26. S. Chen, L. Duan, Q. Kang, Study on propellant management device in plate surface tension tanks. Acta. Mech. Sin. **37**(10), 1498–1508 (2021)
27. P. Concus, R. Finn, On capillary free surfaces in the absence of gravity. Acta Math. **132**, 177–198 (1974)
28. B.J. Carroll, The accurate measurement of contact angle phase contact areas drop volume and Laplace excess pressure in drop on fiber system. J. Colloid Interface Sci. **57**(3), 488–494 (1976)
29. S. Chen, D. Wu, Y. Li, J. Liu, L. Duan, W. Li, Profiles of liquid on the surface of revolution with varying cross-section under microgravity. Microgravity Sci. Technol. **34**, 106 (2022)
30. S. Michielsen, J. Zhang, J. Du, H.J. Lee, Gibbs free energy of liquid drops on conical fibers. Langmuir **27**(19), 11867–11872 (2011)
31. J. Du, S. Michielsen, H.J. Lee, Profiles of liquid drops at the tips of cylindrical fibers. Langmuir **26**(20), 16000–16004 (2010)
32. J. Du, S. Michielsen, H.J. Lee, Profiles of liquid drops at the bottom of cylindrical fibers standing on flat substrates. Langmuir **28**(1), 722–728 (2011)
33. G. Mason, W.C. Clark, Liquid bridges between spheres. Chem. Eng. Sci. **20**, 859–866 (1965)
34. W.C. Clark, J.M. Haynes, G. Mason, Liquid bridges between a sphere and a plane. Chem. Eng. Sci. **23**, 810–812 (1968)
35. M. Fortes, Axisymmetric liquid bridges between parallel plates. J. Colloid Interface Sci. **88**(2), 338–352 (1982)
36. J.W. Honschoten, N.R. Tas, M. Elwenspoek, The profile of a capillary liquid bridge between solid surfaces. American J. Phys. **78**(3), 277–286 (2010)
37. Y. Wang, S. Michielsen, H.J. Lee, Symmetric and asymmetric capillary bridges between a rough surface and a parallel surface. Langmuir **29**(35), 11028–11037 (2013)
38. F.P. Timothy, B.C. James, Asymmetric capillary bridges between contacting spheres. J. Colloid Interface Sci. **454**, 192–199 (2015)
39. E. Reyssat, Capillary bridges between a plane and a cylindrical wall. J. Fluid Mech. **773**, R1 (2015)
40. H.D. Mittelmann, Symmetric capillary surfaces in a cube. Math. Comput. Simul. **35**, 139–152 (1993)
41. D. Langbein, Liquid surfaces in polyhedral containers. Capillary Surfaces. 213–234 (2002)
42. S. Chen, C. Zhang, W. Li, Y. Li, F. Ding, Q. Kang, Capillary phenomena in the corner of truncated-cone-shaped containers under microgravity. Acta Mech. Sin. **39**, 322347 (2023)
43. J.B. Bostwick, P.H. Steen, Stability of constrained capillary surfaces. Annual Review Fluid Mech. **47**(1), 539–568 (2015)